A. Yamagami[1], M. Kajino[1,2], and T. Maki[1]

[1] Meteorological Research Institute (MRI), Japan Meteorological Agency (JMA), Tsukuba, Ibaraki, 305-0052, Japan

[2] Faculty of Life and Environmental Sciences, University of Tsukuba, Tsukuba, Ibaraki, 305-8572, Japan

Corresponding author: Akio Yamagami (yamakami@mri-jma.go.jp)

†Additional author notes should be indicated with symbols (current addresses, for example).

Key Points: 140 characters

- The lower-level troposphere temperature error was correlated with the AOD over Africa and northern South America (R was ~0.6).
- The error was correlated with AOD anomalies over northern South America (China), and direct (direct and indirect) effects were important.
- Operational short-range forecasts experienced common errors associated with yearly and daily aerosol variabilities in these regions.

Abstract (250 words)

This study statistically evaluated the aerosol impact on the temperature error in the lower-level troposphere in short-range numerical weather prediction (NWP). The Global Ensemble Forecast System version 12 (GEFSv12) reforecast exhibited large temperature errors in high-loading areas (North India, Africa, South America, and China). In 1-day GEFSv12 forecasts, the largest average temperature error occurred in the aerosol optical depth (AOD) peak month, and the daily error distribution corresponded to the daily AOD distribution. Even though the temperature error in the 1-day operational forecasts was smaller than that in the GEFSv12 forecasts, the forecast uncertainties in the operational forecasts were comparable to those in 3-day GEFSv12 forecasts over high-loading areas. The daily temperature errors in all NWP models exhibited a correlation coefficient of ~0.5–0.6 for the AOD over Central Africa and northern South America and ~0.3–0.6 for AOD anomalies over China and northern South America. These results indicated that the yearly aerosol variability contributed 25–36% to errors, and the daily variability contributed 10–36% to temperature errors in 3-day forecasts. Although the correlation was low, aerosol impacts also emerged in North India and Central Africa. Partial correlation and composite analysis suggested that the direct effect mainly influenced temperature forecast errors over northern South America, whereas both direct and indirect effects influenced temperature errors over China. Model intercomparison revealed that operational NWP models could experience common forecast errors associated with aerosols in high-loading areas.

Plain Language Summary

Atmospheric aerosols significantly impact weather and climate system via direct (aerosol-radiation interactions) and indirect (aerosol-cloud interactions) effects. Aerosol influences are, however, treated via a monthly climatology (i.e., real-time spatiotemporal variations are not included) in short- to medium-range numerical weather predictions. This study assessed the aerosol influences on temperature forecasts in the lower-level troposphere on short-range timescales. The results indicated that the variability in monthly and daily temperature errors almost corresponded to the aerosol optical depth (AOD) variability in high-loading areas (North India, Africa, South America, and China). The correlation coefficients of the temperature error and AOD ranged from ~0.5–0.6 over central Africa and northern South America, indicating that the yearly aerosol variability contributed ~25–36% to this error. In addition, the correlation between the error and AOD anomalies reached 0.6 over northern South America and 0.3 over China. These results suggested a 10–36% contribution of the daily aerosol variability. Additionally, the direct effect dominated over northern South America, while the both direct and indirect effects were important over China. Model intercomparison in this study revealed that state-of-the-art NWP models are subject to a common error source associated with the aerosol variability in high-loading regions.

1 Introduction

Atmospheric aerosols considerably influence on the weather and climate systems via direct and indirect effects (Haywood and Boucher, 2000; Lohmann and Feichter, 2005). The direct effect entails aerosol-radiation interactions over cloud-free areas, while the indirect effect encompasses aerosol-cloud interactions in cloudy areas. The direct effect indicates aerosol scattering or absorption of short- and long-wave radiation, leading atmospheric warming and cooling depending on the aerosol species, vertical distribution, and environmental conditions. Regarding the indirect effect, aerosols alter cloud properties by functioning as cloud condensation nuclei and ice nuclei. While aerosols enhance the formation of clouds, aerosols can reduce the precipitation efficiency of clouds by preventing the growth of cloud particles. In addition to these two effects, absorbing aerosols impose a certain influence on the atmospheric stability (semidirect effect; Hansen et al., 1997; Lohmann and Feichter, 2001).

Simulations of atmospheric aerosols typically involve various elemental processes, such as primary emission of aerosols and precursor gases, chemical reactions and secondary formation, transportation, dry and wet deposition processes, and aerosol-atmosphere interaction processes. Thus, numerous aerosol simulation studies have been conducted with regional (e.g., Kajino et al., 2019, 2021a; Grell et al., 2005) and global (Bhattacharjee et al., 2018; Gong et al., 2012; Morcrette et al., 2009; Rémy et al., 2019; Tanaka, 2003; Tanaka and Chiba, 2005) models. Regardless of these numerous studies, high uncertainties are associated with each elemental process. To reduce these uncertainties, several approaches have been studied, such as data assimilation to improve the spatiotemporal distribution (Benedetti et al., 2009; Sekiyama et al., 2011; Yumimoto et al., 2016;

Kajino et al., 2021a), the inversion method to improve emissions (Maki et al., 2011; Sugimoto et al., 2010; Yumimoto et al., 2008), and the superensemble method (Kajino et al., 2021b). However, because the solution to all these processes requires very high computational resources, aerosols have been treated in a simple manner in numerical weather prediction (NWP) models.

Aerosol treatment in NWP models depends on the timescale. Whereas aerosols and gas cause high uncertainties (Adebiyi et al., 2020; Thorsen et al., 2020), these components significantly affect the radiation budget on climate timescales. Thus, climate simulations include detailed aerosol processes involving an atmosphere-ocean-land model coupled with an aerosol model. The IPCC (2021) demonstrated that anthropogenic aerosols lowered the global surface temperature from 2010–2019 by 0.0–0.8 K below 1850–1900 levels, while greenhouse gases contributed to warming by 1.0–2.0 K.

On short- to medium-range timescales, forecast skills mainly depend on the accuracy of the initial states (Bauer et al., 2015). Boundary condition and slow-varying atmospheric modes influence forecast skills on subseasonal to seasonal (S2S) timescales (White et al., 2017; Vitart et al., 2017; Vitart and Robertson, 2018). Although the aerosol influence has been addressed based on their climatology at these timescales, this treatment has been updated. Rodwell and Jung (2008) examined the impacts of aerosol climatology replacement from annual fixed values to monthly varying values in the European Centre for Medium-range Weather Forecasts (ECMWF) Integrated Forecasting System (IFS). Their results revealed that the above replacement improved not only surface variables but also global circulations through teleconnections. Bozzo et al. (2020) reported that the replacement of aerosol climatology produced through Copernicus Atmosphere Monitoring Service (CAMS) reanalysis further enhanced Indian monsoon circulation forecasts. The update of aerosol direct effect could improve S2S forecasts (Benedetti and Vitart, 2018). The Japan Meteorological Agency (JMA) Global Spectral Model (GSM) also attained improvement in front and tropical cyclone forecasts by upgrading the aerosol treatment approach (JMA, 2019). Mulcahy et al. (2014) demonstrated that prognostic aerosols under the Coupled Large-scale Aerosol Simulator for Studies In Climate (CLASSIC) scheme reduced the model bias due to dust storm prediction enhancement with the UK Met Office (UKMO) Unified Model (UM). It was further reported that the inclusion of indirect effects improved clouds in high-latitude clean-air regions and strengthened the Indian monsoon circulation and African Easterly Jet. The Korea Integrated Model was also improved by including the indirect aerosol effect (Jeong, 2020).

Despite these aerosol treatment updates, state-of-the-art NWP models cannot adequately predict aerosol impacts. An occasional high-loading event involving dust (Rémy et al., 2015) or biomass burning (Zhang et al., 2016) could notably affect radiation and the surface temperature and lead to forecast errors. The difference in temperature in the lower-level troposphere between reanalysis data (ERA-Interim, Huang et al., 2018; GDAS, Huang and Ding, 2021) and obser-

vations reached up to 2.2 K under highly polluted conditions in North China. Huang and Ding (2021) also the aerosol loading and surface conditions influenced the temperature bias in the lower-level troposphere in 1-day US National Centers for Environmental Prediction (NCEP) Global Forecast System (GFS) predictions.

In these studies, aerosol impacts were evaluated during a short period (shorter than one season) or case study (Rémy et al., 2015) and considering one NWP model (Rodwell and Jung, 2008; Mulcaphy et al., 2014; Bozzo et al., 2020). Zhang et al. (2016) conducted a multimodel comparison, and Huang and Ding (2021) evaluated the aerosol impact during the period from 2016–2018, but their study also involved a case study or one NWP model. Although individual NWP models suffer their own problems, certain forecast errors might be common among these models because most NWP models treat aerosol impacts via the monthly climatology. Additionally, long-term evaluation is desirable because the yearly variability in aerosols is commonly not included. However, long-term simulation at the operational NWP model resolution coupled with sophisticated aerosol schemes is difficult due to the high computational cost. Therefore, this study statistically evaluated the forecast error, especially the temperature error in the lower-level troposphere, associated with the aerosol loading considering multiple prediction datasets and an aerosol reanalysis approaches.

2 Data and Methods

2.1 Aerosol reanalysis dataset

This study employed the aerosol optical depth (AOD) provided by the Japanese Reanalysis for Aerosols (JRAero) v1.0 (Yumimoto et al., 2017) to measure the aerosol distribution and density. JRAero is based on the JMA Earth System Model version 1 (MRI-ESM1) developed by the Meteorological Research Institute (Yukimoto et al., 2012). MRI-ESM1 consists of an atmospheric general circulation model (MRI-AGCM3) and an aerosol transport model, namely, the Model of Aerosol Species IN the Global AtmospheRe mk-2 (MASINGAR mk-2; Tanaka et al., 2003). MRI-AGCM3 exhibits a T159 (~1.1° x 1.1°) horizontal grid spacing and 48 vertical levels. MASINGAR mk-2 calculates the emission, transport, chemical reaction, and removal processes for five major aerosol species (black carbon (BC), organic carbon (OC), mineral dust, sea salt, and sulfate aerosols) and their precursors. MASINGAR mk-2 calculated the AOD at the 550- and 870-nm wavelengths based on the extinction coefficient for each aerosol species at each vertical level. In MRI-ESM1, MASINGAR mk-2 received the required atmospheric field from MRI-AGCM3 and calculated chemical processes. Then, MRI-AGCM3 received aerosol mixing ratio and deposition flux data from MASINGAR mk-2 to calculate radiation modified by the aerosol effect through a coupler. MODIS AOD observations provided by the US Naval Research Laboratory (NRL) and the University of North Dakota were assimilated with 2-D Var into the AOD in JRAero. The observed AOD (two-dimensional) was converted into the three-dimensional mixing ratio based on the predicted vertical profile for each aerosol species. The MODIS AOD was assimilated at 6-hour intervals.

In addition, the predicted horizontal wind and temperature were nudged by linearly interpolated 6-hour JMA operational global analysis (GANAL/JMA; JMA, 2002) data at each timestep (900 s). Tanaka et al. (2003), Yukimoto et al. (2011, 2012), and Yumimoto (2017) provided a detailed description of MRI-ESM1 and MASINGAR mk-2. This study employed the 6-hourly AOD at 550 nm in JRAero from January 2011 to December 2017. Because JRAero assimilates the MODIS AOD and then calculates the contribution of each aerosol species in MASINGAR mk-2 (based on anthropogenic emission inventories, atmospheric variables, and surface conditions), we mainly examine the results based on the total AOD.

2.2 Forecast datasets

We applied the reforecast dataset issued by the NCEP (Zhou et al., 2021) and operational forecasts retrieved from the TIGGE data portal (Swinbank et al., 2016). The ensemble reforecast datasets provided by the NCEP Global Ensemble Forecast System were recently updated to version 12 (GEFSv12). The forecast skill of the geopotential height at 500 hPa of GEFSv12 is comparable to that of the operational GFS, especially up to a lead time of 5 days (Zhou et al., 2019). One of the advantages of reforecast data is that the model configuration remains consistent throughout the period. The improvement in forecast skill arises from the quality of the initial condition due to the increase in assimilated observational data. This study employed GEFSv12 reforecast data initialized at 0000 UTC on each day during the same period matching that of JRAero.

In addition to GEFSv12, we applied operational forecasts of five leading NWP centers: Environmental Climate Change Canada (ECCC), ECMWF, JMA, NCEP, and UKMO. We adopted control forecasts initialized at 0000 UTC on each day during the same period as that of JRAero. As operational systems, the NWP models were updated several times. The TIGGE model description on the ECMWF webpage (https://confluence.ecmwf.int/display/TIGGE/Model+upgrades) provides a detailed model update history, and Yamagami et al. (2018) summarized changes in the model resolution, forecast length, and ensemble size in its Supporting Material. Note that the forecast data of the JMA initialized at 0000 UTC are available after February 2014, and there occur missing data for each NWP center, as mentioned in Yamagami and Matsueda (2021). The treatment method of the aerosol impact in these NWP models is summarized in Table 1. The aerosol climatology is also updated in the ECMWF, JMA, and UKMO systems. In particular, only the UKMO system employed prognostic dust aerosols after February 2015. Most NWP models, however, treated aerosols via a monthly climatology, as mentioned in Section 1.

2.2 Calculation of the forecast error and evaluation of the aerosol impact on the forecast error

We calculated the temperature error of the GEFSv12 forecasts with NCEP FNL data. NCEP FNL data exhibit a grid spacing of 1.0° x 1.0° and a 6-hour

temporal interval. Note that distribution and seasonal cycle of the average temperature error in GEFSv12 calculated with NCEP FNL data was almost similar to that calculated through NCEP GDAS analysis during the same period (July 8, 2015–December 31, 2018) and GFS- and GDAS-based results (Huang and Ding 2021). In the above operational forecasts, their forecast errors were calculated through corresponding control analysis (initial analysis in the control forecast) in a bias-free manner.

Similar to the correlation skill (Yamagami and Matsueda, 2020), the relationship between the temperature forecast error (T_{err}) and AOD was evaluated considering the correlation coefficient $R(T_{err},\ AOD)$ at each grid point as follows:

$$R(T_{\rm err},\ AOD) = \frac{Cov(T_{\rm err},\ AOD)}{\sigma(T_{\rm err}) * \sigma(AOD)},$$

where $Cov(x,\ y)$ and $\sigma(x)$ are the covariance between x and y and the standard deviation of x, respectively. In addition, to estimate the relative importance of aerosol-radiation and aerosol-cloud interactions, the partial correlation coefficient was determined as follows:

$$R(T_{\rm err},\ AOD; cloud) = \frac{R(T_{\rm err},\ AOD) - R(T_{\rm err},\ cloud) * R(AOD, cloud)}{\sqrt{1 - R(T_{\rm err},\ cloud)^2}\sqrt{1 - R(AOD, cloud)^2}},$$

where $R(x,y;z)$ is the partial correlation coefficient between x and y, in which the influence of z is removed. Because JRAero employed atmospheric fields nudged by JMA operational analysis data, we obtained the analyzed total cloud cover (TCC) from Japanese 55-year reanalysis (JRA-55; Kobayashi et al., 2015) data.

Table 1. Treatment of aerosols in the operational NWP models.

@ >p(- 4) * >p(- 4) * >p(- 4) * @

Center

& Period & Aerosol treatment

ECCC

& Jan. 2011 & AOD of Toon and Pollack (1976) distributed across the first 1500 m above the surface.

ECMWF
(Bozzo et al. 2020)

& Jan. 2011–Jul. 2017 & Five aerosol types (dust, organic matter, sulfate, black carbon and maritime aerosols); monthly average and total integrated AODs based on Tegen et al. (1997).
& Aug. 2017 & Five main aerosol types (dust, in three size bins; organic matter; sulfate; black carbon; and sea salt, in 3 size bins) of the CAMS.

JMA
(JMA 2019)

& Feb. 2014–May. 2017 & Monthly average climatological AOD created based on MODIS, MISR, and OMI observations.
& Jun. 2017 & Five aerosol types (dust, in three size bins; organic carbon; sulfate; black carbon; and maritime aerosols, in two size bins); 3-D monthly average climatology via the MASINGAR mk-2 model with modification based on the observed climatology.

NCEP
(Lu et al., 2013, NCEP Office Note 472)

& Jan. 2011 & Prescribed aerosol distributions based on a global climatological aerosol database (Hess et al., 1998).
& &

UKMO
(Mulcahy et al., 2014, Kolusu et al., 2015)

& Jan. 2011–Jan. 2015 & Eight aerosol types (dust, sulfate, biomass burning, fossil fuel black carbon, fossil fuel organic carbon, sea salt, nitrate, and secondary organic aerosols); monthly mean three-dimensional climatologies of the mass mixing ratio created with the CLASSIC algorithm.
& Feb. 2015 & Monthly mean three-dimensional climatologies of the mass mixing ratio, except for mineral dust for which the mixing ratio is prognostic (2 bins) based on Woodward (2001).

3 Results

3.1 Temperature error in the lower-level troposphere in the GEFSv12 dataset

The monthly mean forecast error in the temperature at the 850 hPa level at a lead time of 1 day in GEFSv12 exhibited different seasonal cycles over individual regions (Fig. 1). In northern India, a positive error of ~1.5 K was observed from late spring to early autumn. This error occurred over northeastern India in May (Fig. 1e) and was extended to northeastern India from June to September (Fig. 1f–i). A positive error also emerged over equatorial Africa in both winter (Fig. 1a, b, and l) and summer (Fig. 1f–i). In South America, a positive error occurred in the northern part in September (Fig. 1i) and the southern part in February (Fig. 1b). A positive error was also observed in February over China (Fig. 1b). In contrast, a negative error occurred near the Tibetan Plateau and Rocky Mountains throughout the year. The difference in topography resolution between the GEFSv12 and NCEP FNL models could contribute to this negative error. In addition, a negative error was observed over the ocean. The negative bias over the ocean, except for the Southern Pacific and Indian Oceans, disappeared when the error was calculated over the period from July 2015–December

2018, indicating that this negative error arose from period extension to 2011–2017. This study focused on the positive errors over northern India, northern and equatorial Africa, northern and southern South America, and China at a monthly mean error larger than 0.5 K during the peak month (Fig. 2). Note that the areas of North Africa (N. Africa in Fig. 2) and China were defined by the error at 925 hPa because the error at 925 hPa was larger than that at 850 hPa.

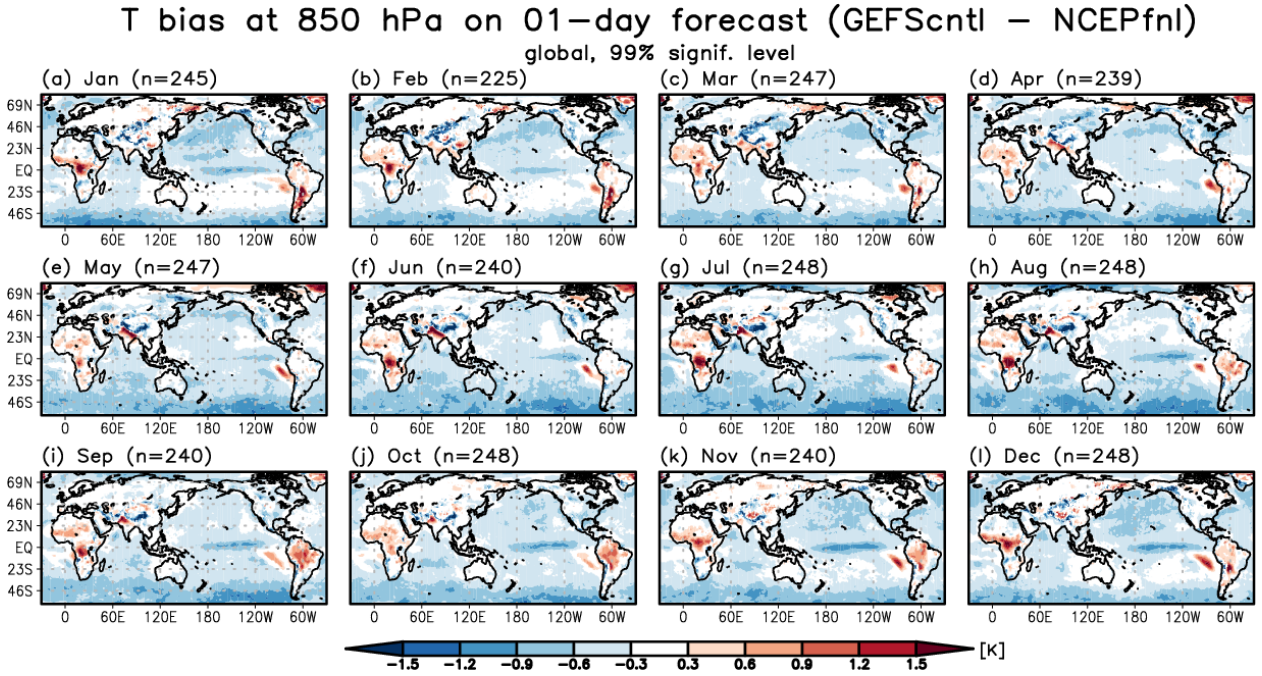

Figure 1 Monthly mean 1-day forecast error in the temperature at 850 hPa in GEFSv12 during the period from 2011–2017. Errors with a statistical significance at the 99% confidence level are shaded.

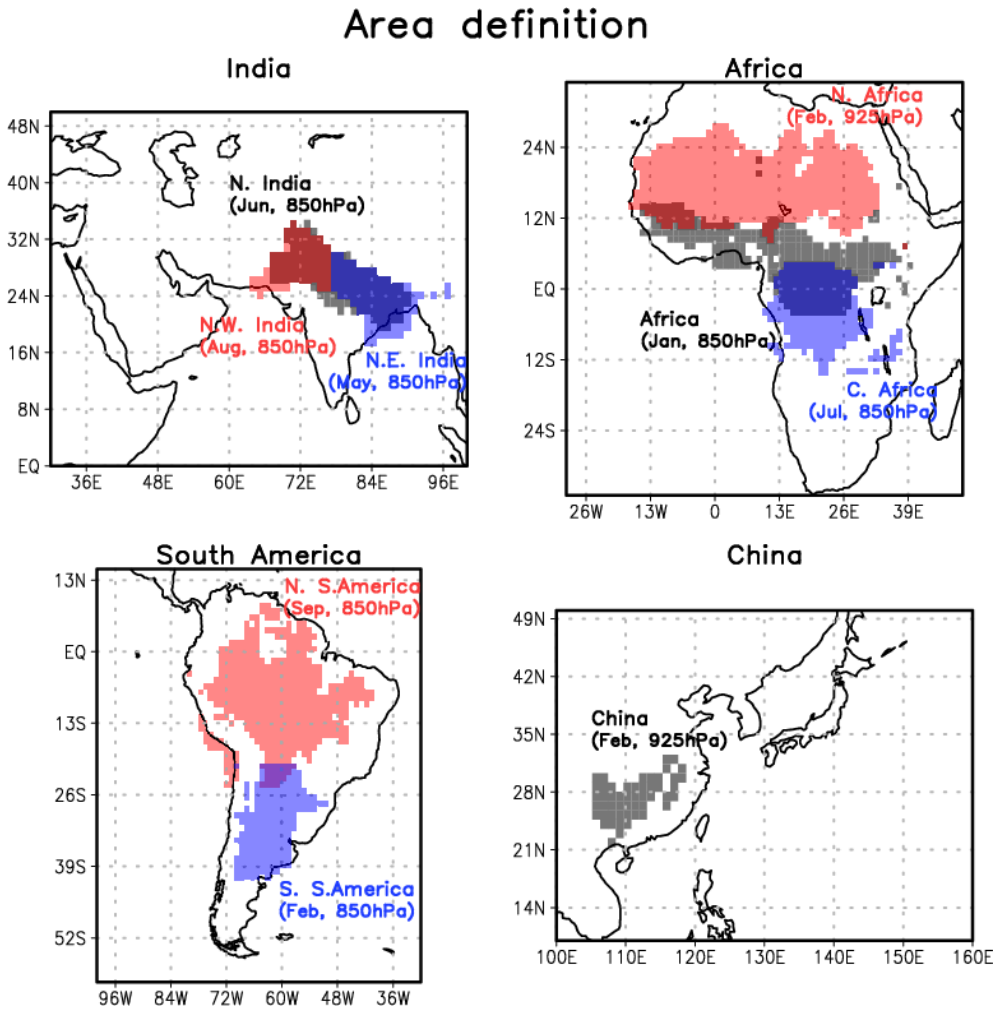

Figure 2 Definition of each area. The shading in each area satisfies the condition that the monthly mean temperature error is larger than 0.5 K in the 1-day GEFSv12 forecasts at a certain level and month (described above or below each shaded area).

3.2 Variability in the temperature error and AOD

The monthly variability in the AOD over northern India indicated two peaks in early summer and winter (Fig. 3a-c). In northern India (Fig. 3a), one of the peaks reached 0.47 in June, and the other reached 0.46 in January. While the seasonal cycle of the AOD in northeast India was similar to that in northern India, the seasonal cycle in northwest India attained the highest value in July (~0.49). Similar to the temperature error (Fig. 1), the AOD peak also shifted from east to west across northern India from May–September. In Africa, the climatological AOD was the highest in winter (Fig. 3d). The peak reached 0.59

in February, followed by a value of 0.43 in June and July and 0.42 in January and December. In northern Africa, the AOD exhibited a rapid increase from January to February and the highest value in May (Fig. 3e). In contrast, the AOD in Central Africa (Fig. 3f) revealed two peaks in August (~0.63) and in February (~0.43), and the amplitude was larger than that in northern Africa. The seasonal cycle of the AOD was almost consistent with that of the temperature error in these three areas. The monthly variability in the AOD attained a peak in September in both North (~0.39, Fig. 3g) and South America (~0.22, Fig. 3h). While the highest AOD in September corresponded to the largest temperature error in the northern part, there occurred no AOD peak in February in the southern part. In China, the AOD was apparently higher than in the other areas, and the peak value reached 0.95 in March, followed by a value of 0.76 in January and April (Fig. 3i). Overall, the peak month of the AOD corresponded to that of the temperature error in all areas, except for the northern part of Africa and the southern part of South America, suggesting that a higher aerosol loading is one of the possible sources for the temperature error in the lower-level troposphere.

The distribution of the daily temperature error corresponded to that of the daily AOD in each area (Fig. 4). In particular, the relationship was clear in the African regions (Fig. 4d-f). For example, the median AOD was higher in 2012 and 2016 in Africa, and the median daily temperature error was also larger in these years (Fig. 4d). This result indicates that the number of high-loading days corresponded to that of large-error days. Thus, a higher aerosol loading could lead to a larger temperature error. A similar relationship was observed in northern India (Fig. 4a), the northern part of South America (Fig. 4g), and China (Fig. 4i). In addition to the median value, the 90^{th} percentile values of the temperature error corresponded to those of the AOD. For example, the higher 90^{th} percentile values in northwest India (Fig. 4b), North Africa (Fig. 4e), and Central Africa (Fig. 4f) corresponded to the broad distribution of the daily temperature error in 2015, 2012, and 2011, respectively. Interestingly, the relationship was notable in the southern part of South America, where the peak month of the temperature error did not correspond to that of the AOD (Fig. 3h). Therefore, occasional high-loading events could lead to a high forecast uncertainty in lower-level tropospheric temperatures.

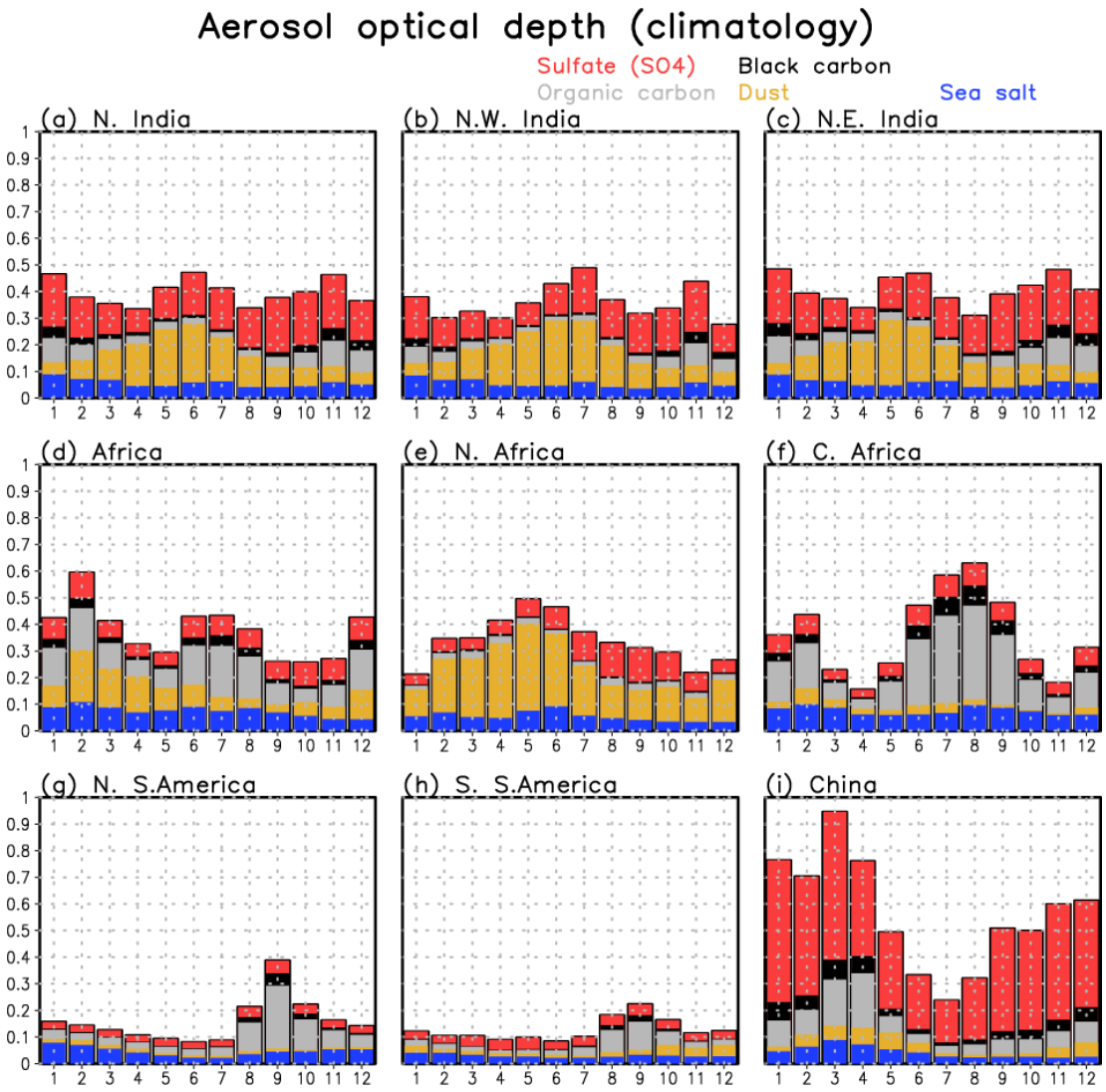

Figure 3 Average monthly variability in the AOD in each area. Red, black, gray, yellow, and blue indicate the contributions of sulfate, black carbon, organic carbon, dust, and sea salt, respectively.

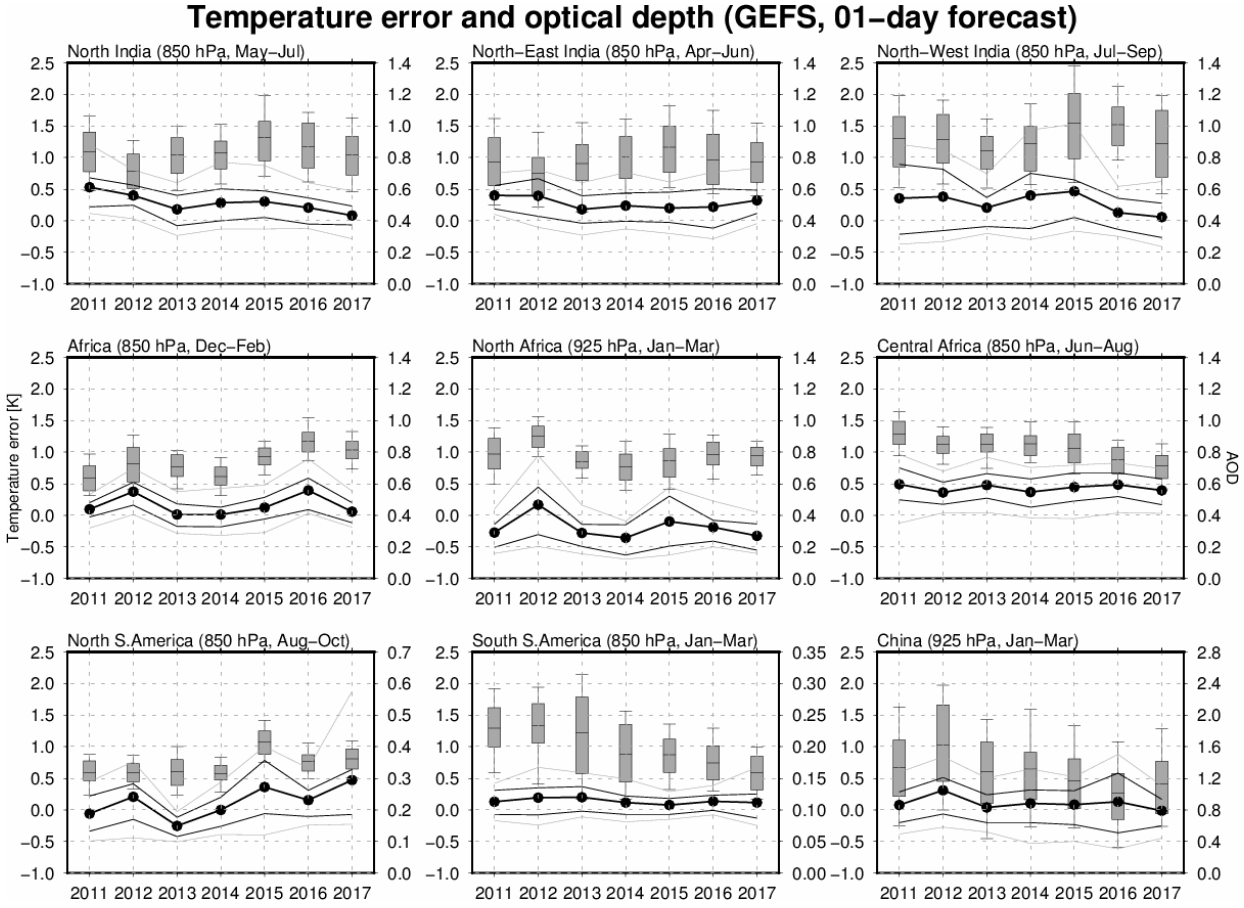

Figure 4 Distribution of the temperature error in the 1-day GEFS forecasts (box plot, left axis) and AOD (lines, right axis) in the 3 months (described in each panel). The horizontal bar in the box (the bold black line with a black circle) indicates the median value of the temperature error (AOD). The box limits (thin black lines) indicate the range of the 25^{th} and 75^{th} percentile values of the temperature error (AOD), and the vertical lines extending from the box (thin gray lines) indicate the range of values from the 10^{th} to 90^{th} percentiles of the temperature error (AOD).

3.3 Comparison of the temperature error among the various NWP centers and its relationship to the AOD

Intermodel comparison of the temperature error revealed that the errors in the GEFSv12 and NCEP forecasts were larger than those in the forecasts of the other NWP centers (e.g. over north India; Fig. S1a-c) and some errors were specific to the GEFSv12 (and NCEP) forecasts at a lead time of 1 day (Fig. S1). The temperature error, however, reached 0.5 K in the 3-day forecasts of the other centers in North India (Fig. 5a–c), the northern part of South America

(Fig. 5g), and China (Fig. 5i). In these areas, while the average error was larger in the GEFSv12 forecasts than that in the forecasts of the other NWP centers, the daily error distribution of the other NWP centers was comparable to that in the GEFSv12 forecasts (the bars in Fig. 5). These results indicated that the uncertainties in the temperature forecasts were prominent in these high-loading areas across all NWP centers.

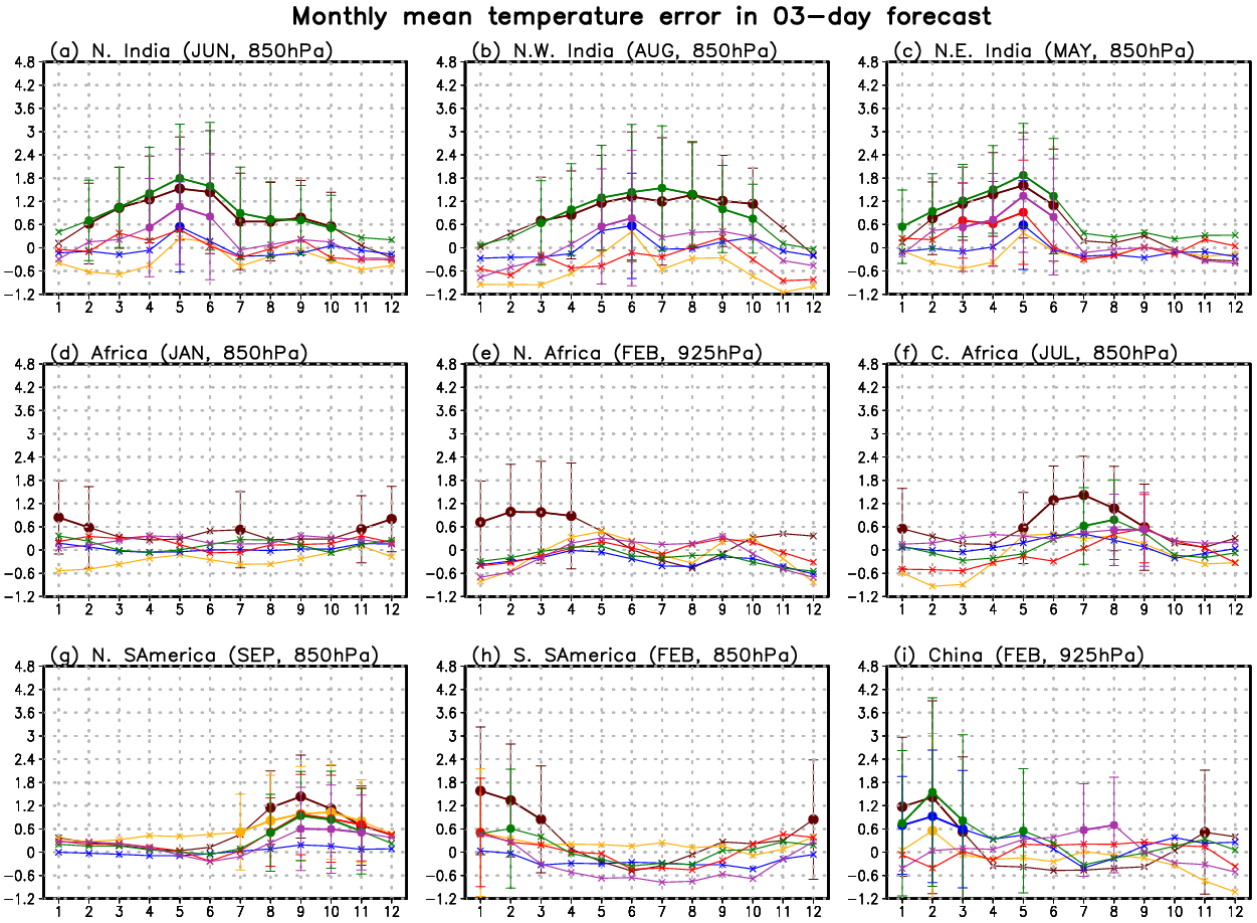

Figure 5 Monthly mean temperature error in the 3-day forecasts of the GEFS (brown), ECCC (yellow), ECMWF (blue), JMA (red), NCEP (green), and UKMO (purple) in the defined area in Fig. 2. The filled circles and error bars indicate the average error larger than 0.5 K and 1 standard deviation, respectively.

The correlation coefficient between the temperature error in the 3-day forecasts and AOD was notable over Central Africa and northern South America (Fig. 6). The correlation coefficient reached 0.5 over Central Africa and 0.6 over Northern South America for the GEFSv12 forecasts (Fig. 6a). A positive correlation

indicated a large temperature error on higher-loading days (i.e., the predicted temperature was higher than the observed temperature). Thus, a positive correlation could correspond to a decrease in the analyzed (observed) temperature due to aerosols. All NWP centers showed a similar correlation coefficient distribution in these areas, except for the ECMWF and UKMO over Central Africa (Fig. 6b–f). In addition, the correlation coefficient reached ~0.3 over China and Australia in general across all centers, except for the JMA. The correlation coefficient indicated that approximately 10–36% of the temperature error in the lower-level troposphere was associated with the aerosol variability. Because the monthly variability in the AOD was treated in most of the NWP models (Table 1), the forecast error might be associated with the yearly variability in the AOD and the bias in the AOD climatology in each NWP model. The update of the aerosol climatology in the ECMWF (Bozzo et al., 2020), JMA (JMA, 2019), and UKMO (Mulcahy et al., 2014) models influenced the temperature and radiation over Central Africa and the circulation of the Indian monsoon. The correlation coefficient value of ~0.3 near the Arabian Peninsula for the ECCC and UKMO forecasts and around Southeast Asia for the JMA and UKMO forecasts might be related to the circulation change associated with the dust aerosol variability. Therefore, consideration of the yearly variability in aerosols could further increase the temperature forecast skill in short- to medium-range forecasts in high-correlation areas, in addition to improving the monthly climatology.

The daily aerosol variability was also not treated in all NWP models, except for dust aerosols in the UKMO model after February 2015 (Table 1). To evaluate the contribution of the daily aerosol variability, we calculated the correlation coefficient between the temperature error and AOD anomalies (Fig. 7). The high correlation coefficient over Central Africa and northern South America disappeared. However, a correlation coefficient of ~0.3 emerged over northeast South America and China across all NWP centers in general. These results indicated that the temperature forecast skill could improve across all NWP centers by treating the daily aerosol variability over northeast South America and China. In particular, the correlation coefficient reached 0.6 over northeast South America from July–November (contour in Fig. 9). Thus, the treatment of daily aerosols could lead to an improvement in the temperature forecast error of ~36% in these months.

A correlation coefficient of zero does not necessarily indicate that aerosols exert no impact on the temperature forecasts in the other areas (Fig. 8). Although each model experienced a different temperature bias in each area, the forecast errors on high-loading days were generally larger than those on low-loading days over Northwest India and Central Africa across all models (Fig. 8b and f). Similar positive differences also emerged over northern India in the ECCC, ECMWF, and JMA forecasts and over southern South America in the GEFSv12 and ECCC forecasts. These results indicated that occasional high-loading events could increase the temperature error in these areas. In contrast, a small or negative difference indicated the low impact of the daily aerosol variability or higher impact of other processes on temperature forecast errors. Consistent

with Fig. 7, the forecast error was larger on high-loading days than that on low-loading days over northeast South America and China (Fig. 8g and i). In northeast South America (China), the difference in error ranged from 0.1–0.6 K (0.6–1.5 K) between high- and low-loading days with a 0.3 (1.0) AOD anomaly difference. Thus, the impact of aerosols on the temperature forecast error ranged from approximately 0.3 to 2.0 K/AOD. These results are relatively consistent with the values estimated by Zhang et al. (2016).

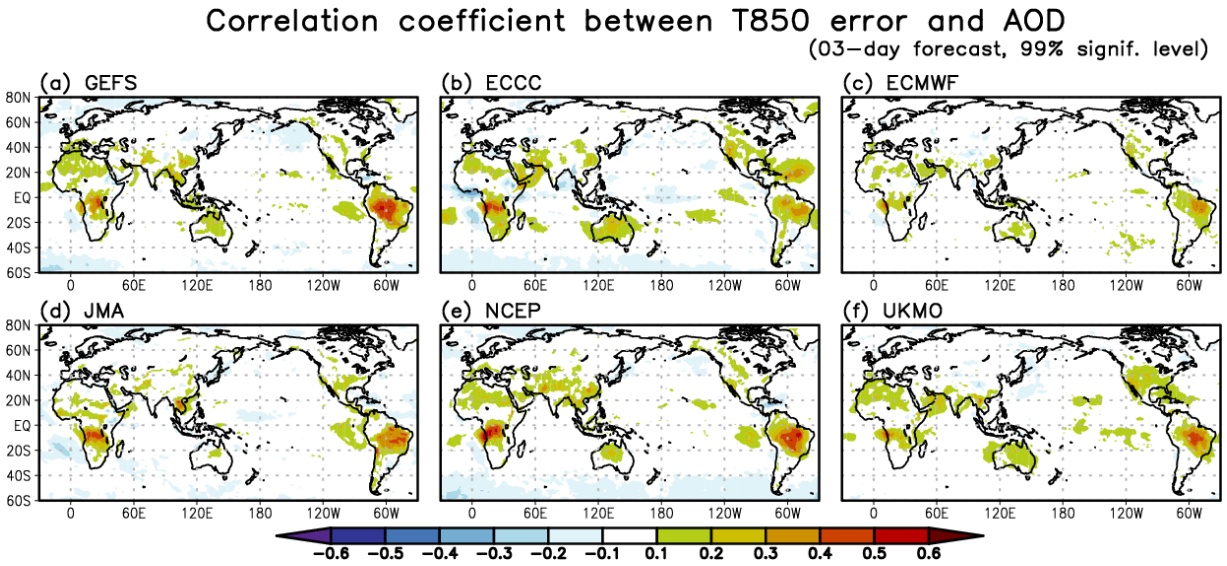

Figure 6 The correlation coefficient between temperature error in the 3-day (a) GEFS, (b) ECCC, (c) ECMWF, (d) JMA, (e) NCEP, and (f) UKMO (purple) forecasts and AOD.

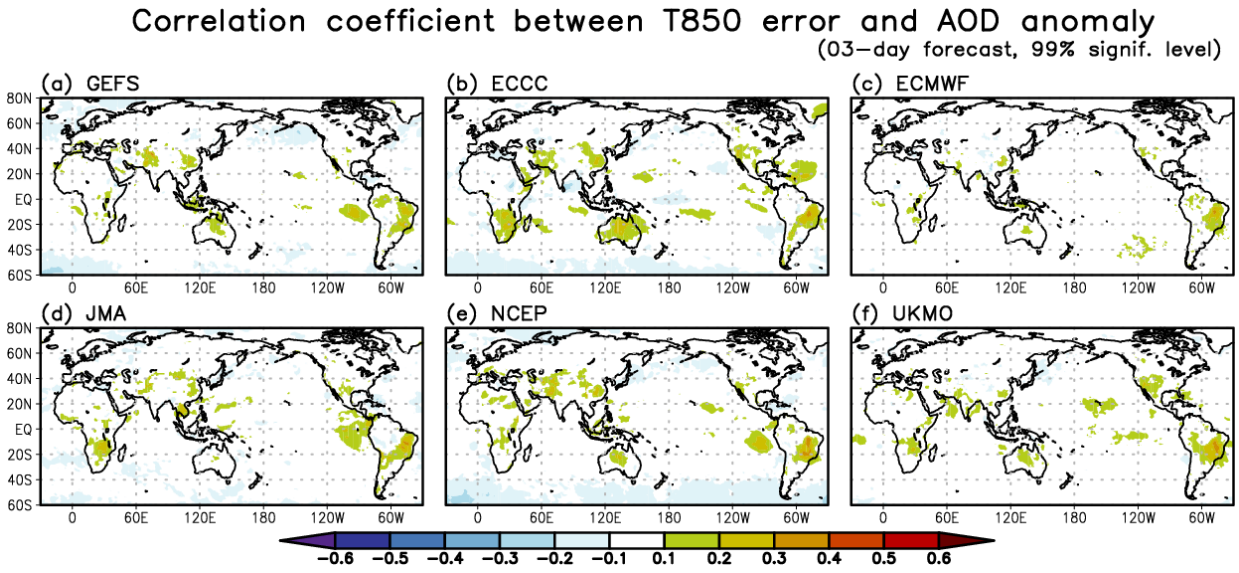

Figure 7 Similar to Fig. 6 but for the AOD anomalies.

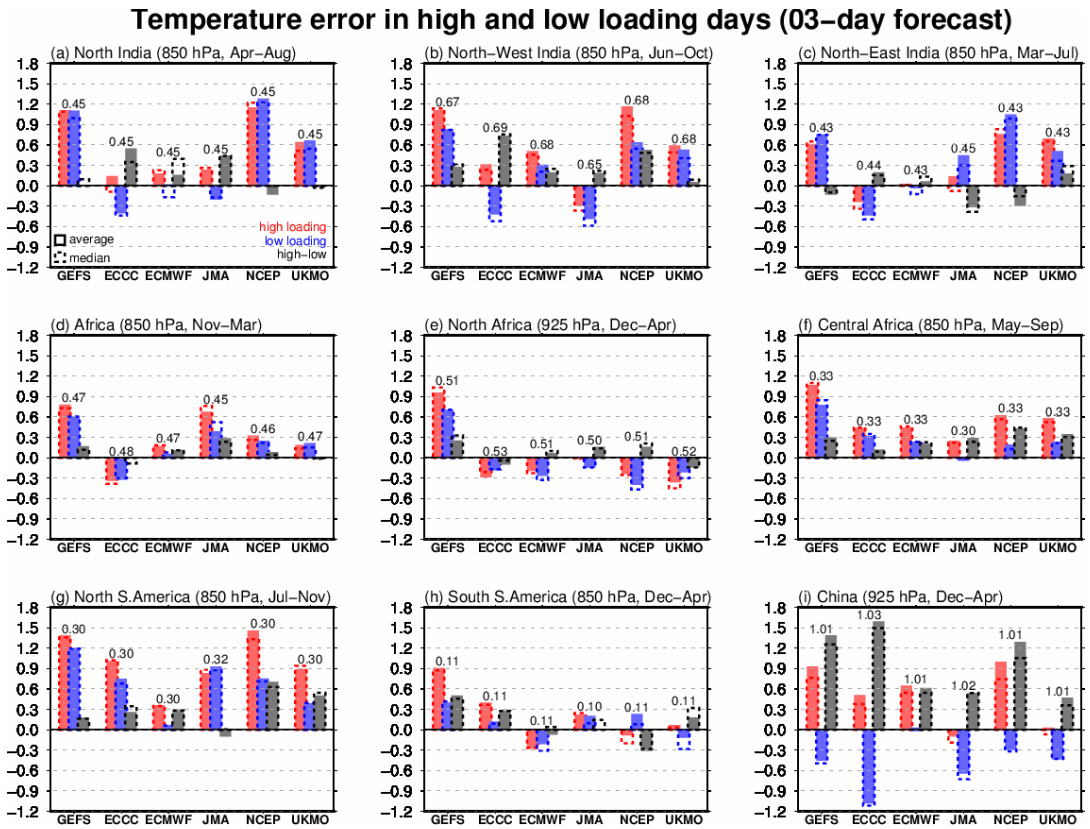

Figure 8 Average (shaded) and median (broken line) values of the area-averaged temperature forecast error on high- (AOD anomaly $>75^{\text{th}}$ percentile value, red) and low-loading (AOD anomaly $< 25^{\text{th}}$ percentile value, blue) days and their difference (high-low, gray). The difference in the average AOD is provided above the bars (high-low).

3.4 Contribution of the direct and indirect effects over northeast South America and China

Aerosols can generate both direct and indirect effects. We employ partial correlation coefficient (Figs. 9 and 11, respectively) and composite analyses (Figs. 10 and 12, respectively) to estimate the relative importance of these effects over northeast South America and China. The partial correlation coefficient could evaluate the relationship between the temperature error and AOD anomalies without TCC influence. The partial correlation coefficient (shading in Fig. 9) was almost similar to the original correlation coefficient (contour), indicating that the TCC imposed little influence on the relationship between the temperature error and AOD over northeast South America. In particular, the partial correlation coefficient nearly matched the original correlation coefficient over central Brazil. This result suggested the dominance of aerosol-radiation interactions in this area. On average, GEFSv12 exhibited a positive error of ~1.2 K over Brazil on large-error days (upper 25^{th} percentile of the temperature error, Fig. 10a). The predicted TCC was higher on high-loading days than that on low-loading days in the southern part of Brazil (Fig. 10b). Consistent with the high TCC, the downward shortwave radiation at the surface (DSW) was lower on high-loading days than that on low-loading days. These results indicated that higher aerosol loadings induced a higher TCC and lower DSW in the southern part of Brazil (Fig. 10c). The all-sky DSW in the JRAero data was lower on high-loading days than that on low-loading days in this area, similar to the GEFSv12 forecasts (Fig. 10f). Thus, GEFSv12 correctly predicted the DSW decrease due to the TCC increase in the southern part of Brazil. In addition, the analyzed clear-sky DSW revealed a notable negative difference in the JRAero data (Fig. 10e) in central Brazil, where the difference in the AOD was the largest (0.2, Fig. 10d). Because JRAero does not provide radiation at the top of the atmosphere, we could not reveal the relationship between the radiation budget difference and temperature error. However, similar to the relationship between the temperature difference and AOD, as shown in Fig. 8, the difference in the clear-sky DSW of ~100 W/m^2/AOD is consistent with the results of Zhang et al. (2016). Additionally, the difference in the DSW between high- and low-loading days (~30 W/m^2) was similar to the aerosol impact on the DSW calculated by Mulcuphy et al. (2014). The partial correlation coefficient and composite fields suggested that part of the temperature error was associated with the direct effect, especially in the northern part of Brazil. The temperature error over northeast Brazil was independent of the relative humidity (RH) at 850 hPa and TCC (Fig. S3), supporting that the direct effect caused the temperature error. Biomass burning could constitute one of the main contributors to the temperature error (Kolus et al., 2015; Thornhill et al., 2018).

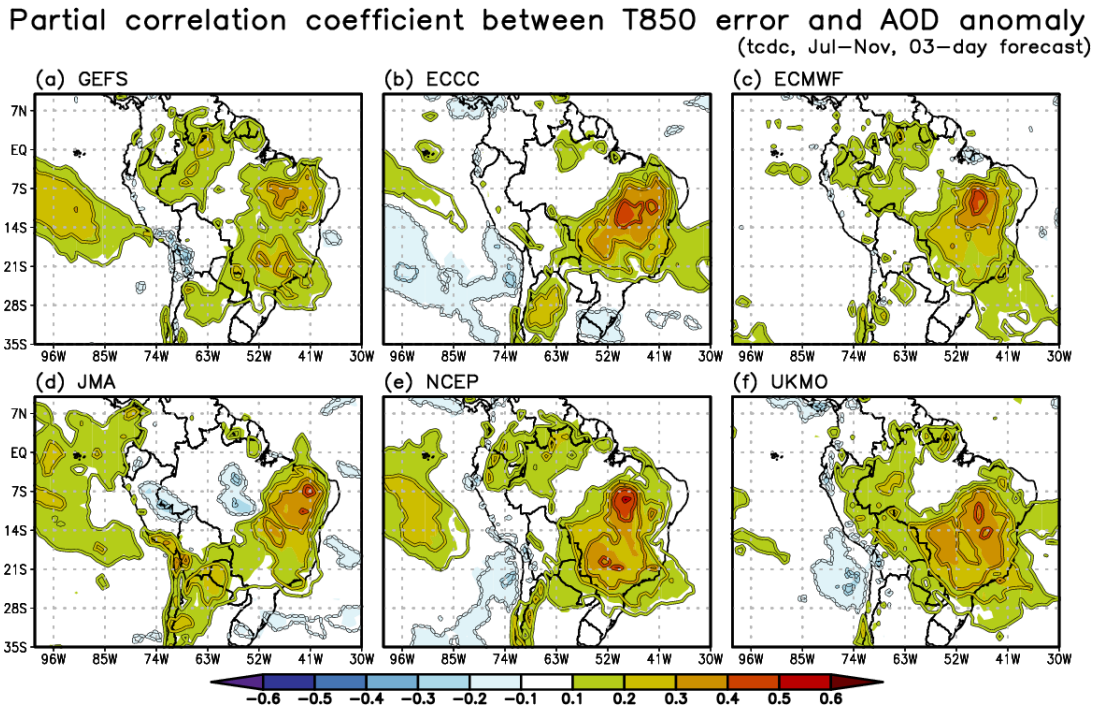

Figure 9 (Contours) Similar to Fig. 6 but from July to November in South America. (Shading) The correlation coefficient between the temperature error and AOD anomalies in which the forecast error explained by the TCC variability is removed through partial correlation analysis.

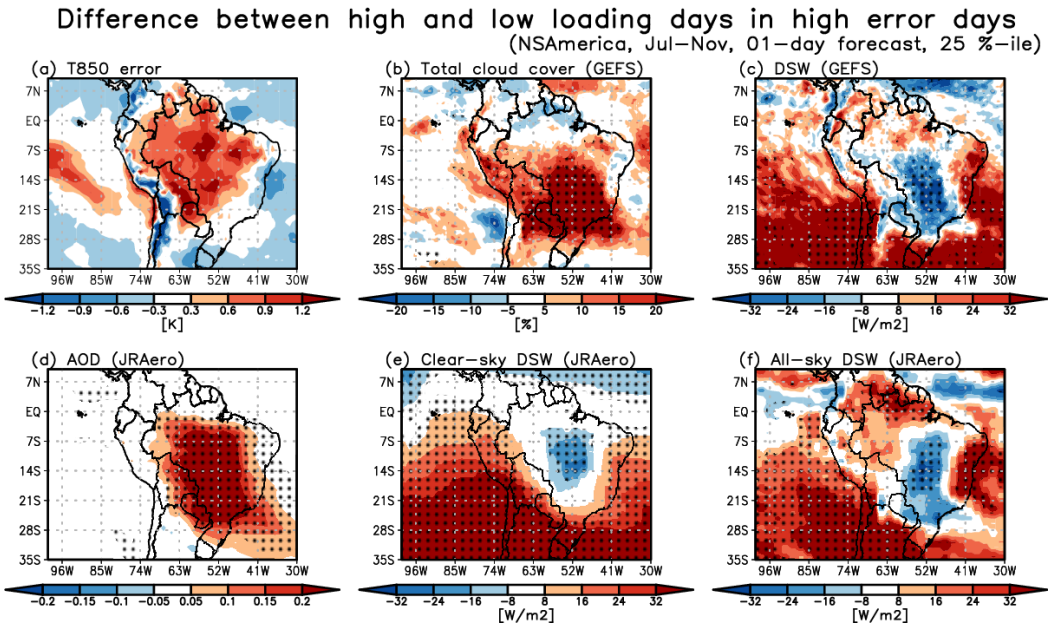

Figure 10 (a) Average temperature error on the large-temperature error days (high+low-loading days). (b-f) Difference in the predicted (b) TCC and (c) all-sky downward shortwave radiation at the surface values between high- and low-loading day composite (high-low) forecasts in GEFSv12 and (d-f) that in the analyzed (d) AOD, (e) clear-sky downward shortwave radiation, and (f) all-sky downward shortwave radiation at the surface (shading). The stippled line indicates the difference with a statistical significance at the 99% confidence level.

In contrast to the northern part of South America, the partial correlation coefficient (shading in Fig. 11) was 0.1 lower than the original correlation coefficient over China from December to April across all centers, suggesting that the temperature error was related to AOD anomalies through the TCC. Based on the composite fields on large-error days, GEFSv12 yielded a positive error of 1.2 K in the southern part of China (Fig. 12a). While the predicted TCC was higher on high-loading days than that on low-loading days in the central to northern parts, the difference was small and statistically insignificant in the southern part (Fig. 11b). The difference in the DSW was negative in Central China but reached almost zero near the southern part of China (Fig. 12c). These results suggest that GEFSv12 predicted the increase in TCC and the associated decrease in DSW from northern to Central China. Nevertheless, there occurred no difference in DSW predictions along the southern coast of China between high- and low-loading days. In JRAero, a significant difference in the AOD of 0.2 was observed across all of China, including along the southern coast (Fig. 12d). Associated with the AOD difference, the all-sky DSW exhibited a significant negative difference (approximately -30 W/m^2, Fig. 12f). The clear-sky

DSW contributed to the difference in the all-sky DSW in Central China, but the contribution was relatively small near the edge of the all-sky DSW difference (Fig. 12e). In addition, the temperature error was insignificant at a lower RH at 925 hPa and under TCC conditions (Fig. S5). These results suggest that GEFSv12 did not suitably predict clouds near the southern part of China on high-loading days, resulting in a positive temperature forecast error.

Because the TCC resulting from reanalysis contains a high uncertainty (Free et al., 2015; Miao et al., 2019). we calculated the partial correlation coefficient using the TCC retrieved from ERA5 (Hersbach et al., 2020). The ERA5 results were similar to those of JRA-55 over northern South America (Fig. S2) and China (Fig. S4). Therefore, the indirect effect could yield an as large contribution as that of the direct effect to the temperature forecast error along the southern coast of China.

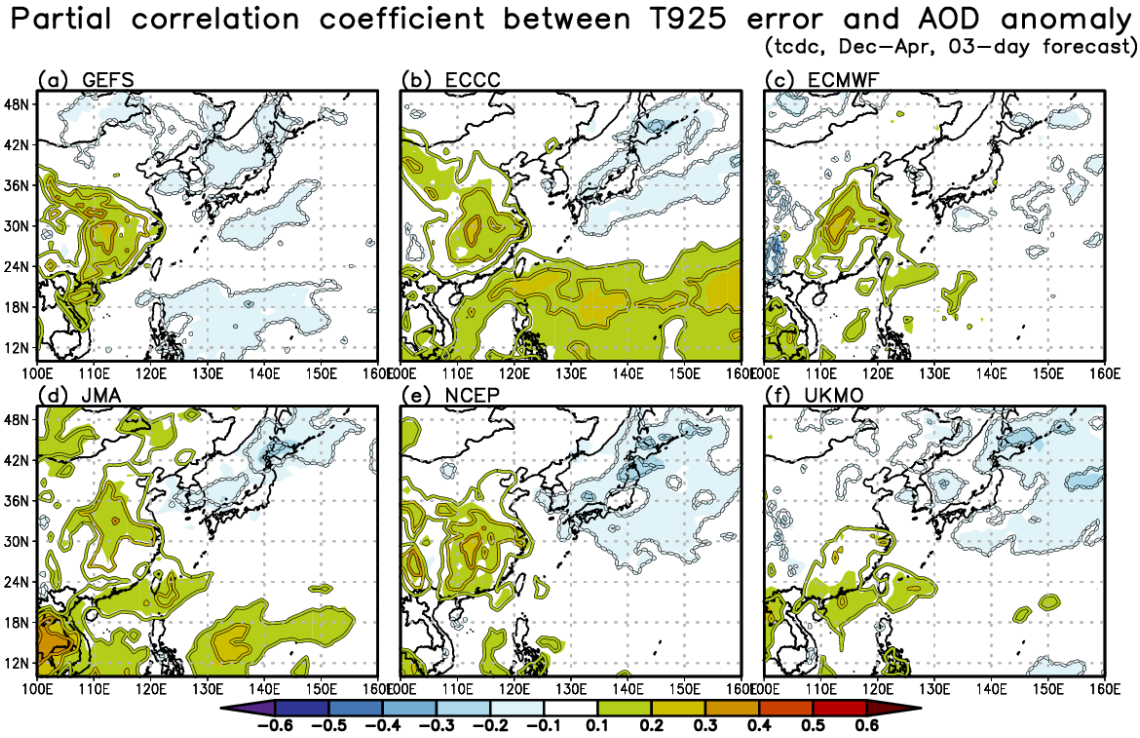

Figure 11 Similar to Fig. 9 but for China.

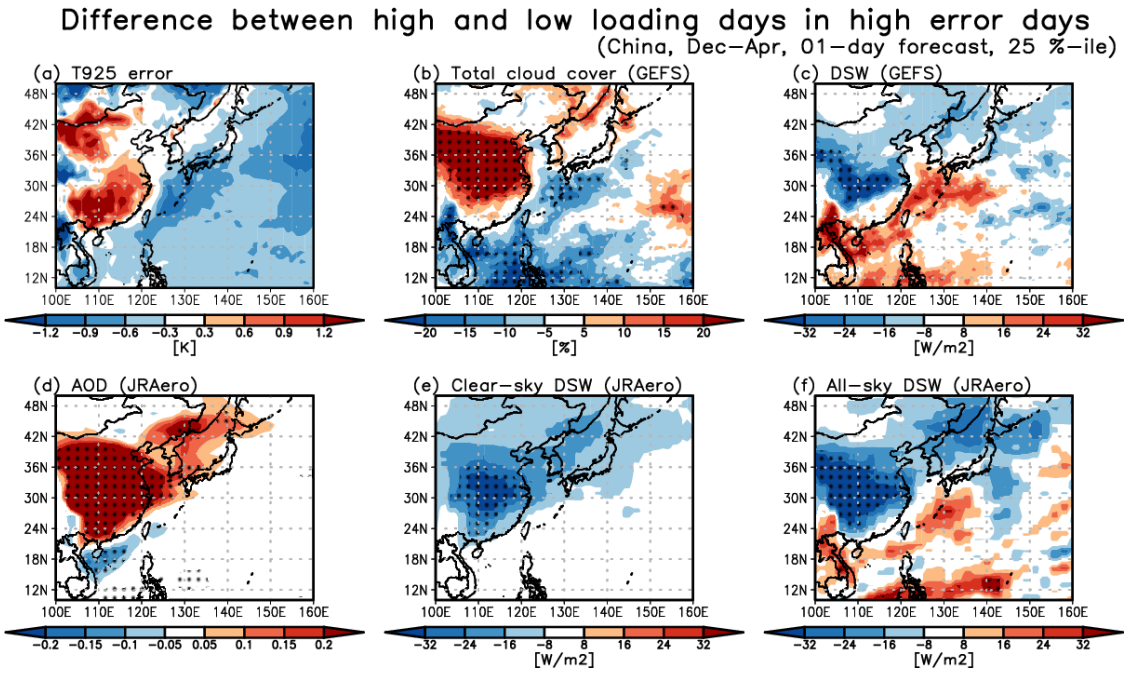

Figure 12 Similar to Fig. 10 but for China.

4 Summary and Conclusion

In this study, we statistically evaluated the aerosol impact on the temperature error from 2011–2017 considering JRAero and GEFSv12 reforecast and five operational forecast datasets (ECCC, ECMWF, JMA, NCEP, and UKMO). This study focused on northern India, northern to Central Africa, South America, and China, where the 1-day GEFSv12 forecast exhibited a large temperature error. The positive temperature error in northern India was the largest in June, and the error shifted from east to west from May to September. The temperature error was the largest in Central Africa in January and July and in North Africa in February. The GEFSv12 forecast also exhibited the largest forecast error in February over China. The peak month of the temperature error was generally consistent with that of the AOD in each region, except for Central Africa and southern South America. In addition, the daily temperature error distribution corresponded to the daily AOD distribution in each year in all regions.

Although these results were relatively consistent with a previous study of Huang and Ding (2021), the 1-day operational forecasts, except for those of the NCEP, indicated a much smaller temperature error than that in the GEFSv12 forecast. The temperature error in the operational forecasts increased in the 3-day forecasts, and the daily variability reached as high as that in the GEFSv12 forecast in northern India, Central Africa, northern South America, and China. Therefore, the forecast uncertainty in the lower-level troposphere is high in these

areas, and aerosol loading could represent one of the reasons for this forecast uncertainty.

The correlation coefficient between the daily temperature error and AOD reached ~0.6 over Central Africa and northern South America across all NWP centers, indicating that ~36% of the temperature error was related to the AOD throughout the year in these regions. The correlation coefficient increased in specific months (e.g., May to September over northern India) and for specific aerosol species (e.g., the AOD of mineral dust yielded a correlation coefficient of ~0.6 over northern India, Fig. S6). Thus, the impact of aerosols on temperature forecasts largely depended on the season, region, and aerosol species. The operational NWP models treated only the monthly variability via the climatology of aerosols. Hence, some of the temperature error could be associated with the yearly variability in aerosols. In addition, the aerosol climatologies created from aerosol models and observations could include high uncertainties (Session et al., 2015; Andrews et al., 2018). Therefore, the aerosol climatology should be further improved, which could reduce these temperature errors.

The correlation coefficient between the temperature error and AOD anomalies reached ~0.6 over northern South America from July to November and ~0.3 over China from December to April, indicating that the temperature error ranging from 10–36% was associated with the daily aerosol variability in these regions. Whereas aerosol-radiation interactions mainly influenced the temperature error over northern South America, both direct and aerosol-cloud interactions influenced the error over China. These results indicated that the relative importance of the direct and indirect effects varied among the individual regions. Although the change in the effective radius of hygroscopic aerosols was treated in certain NWP models, aerosol-cloud interactions were not considered in any of the NWP models. Mulcahy et al. (2014) reported that the zonal mean cold bias below 700 hPa could be improved by including aerosol indirect effects in 5-day UKMO forecasts. The results in this study suggested that the treatment of indirect effects could further impact high-loading regions, such as China. In addition, only the UKMO model employed prognostic dust aerosols in the upgrade process of the aerosol treatment in 2015. This could be related to the smaller difference in the temperature error between high- and low-loading days in the UKMO forecasts than that in the forecasts of the other centers over northern India.

The statistical analyses in this study are consistent with the fully coupled experiments conducted in previous studies (e.g., Rodwell and Jung 2008; Bozzo et al., 2020; Mulchahy et al., 2014). Model intercomparison revealed that certain temperature forecast errors were common issues among the considered NWP models, and some of these errors were associated with the yearly and daily aerosol variabilities. This study further suggested the importance of including the indirect effect on short- to medium-range forecasts in specific areas. However, this statistical analysis could not separate the impacts of aerosols between the increase in effective radius or the increase in concentration. Further studies

targeting both the observation and modeling of aerosols are desired to reduce these forecast errors in operational NWP models by improving the aerosol treatment approach.

Acknowledgments

The authors thank the ECMWF for providing the TIGGE and ERA5 datasets and the NCEP for providing the GEFSv12 and NCEP FNL datasets. The authors are also grateful to the MRI and University of Kyushu for providing the JRAero and JRA55 reanalysis datasets. This study was supported by the Fundamental Technology Research of the MRI (M5), the Integrated Research Program for Advancing Climate Models (TOUGOU), the Environmental Restoration and Conservation Agency (ERCA), the Environment Research Technology Development Fund (JPMEERF20215003 and JPMEERF20205001), and the Japanese Society for the Promotion of Sciences (JSPS) KAKENHI grant no. JP19H01155.

Open Research

The JRAero dataset can be obtained upon data request from the developers (https://www.riam.kyushu-u.ac.jp/taikai/JRAero/index.html). The operational ensemble forecast datasets are available at the TIGGE data portal (https://apps.ecmwf.int/datasets/data/tigge/levtype=sfc/type=cf/), and the GEFS version 12 ensemble reforecast can be obtained from Amazon Web Services (https://noaa-gefs-retrospective.s3.amazonaws.com/index.html). The reanalysis datasets of JRA-55 (https://jra.kishou.go.jp/JRA-55/index_ja.html) and NCEP FNL (doi:10.5065/D6M043C6) and ERA5 (doi:10.5065/D6X34W69) reanalyses are also available at https://reanalyses.org/.

References

Adebiyi, A. A., Kok, J. F., Wang, Y., Ito, A., Ridley, D. A., Nabat, P., & Zhao, C. (2020). Dust Constraints from joint Observational-Modelling-experiMental analysis (DustCOMM): Comparison with measurements and model simulations. *Atmospheric Chemistry and Physics*, *20*(2), 829–863. https://doi.org/10.5194/acp-20-829-2020

Andrews, E., Ogren, J. A., Kinne, S., & Samset, B. (2017). Comparison of AOD, AAOD and column single scattering albedo from AERONET retrievals and in situ profiling measurements. *Atmospheric Chemistry and Physics*, *17*(9), 6041–6072. https://doi.org/10.5194/acp-17-6041-2017

Bauer, P., Thorpe, A., & Brunet, G. (2015). The quiet revolution of numerical weather prediction. *Nature*, *525*(7567), 47–55. https://doi.org/10.1038/nature14956

Bhattacharjee, P. S., Wang, J., Lu, C., & Tallapragada, V. (2018). The implementation of NEMS GFS Aerosol Component (NGAC) Version 2.0 for global multispecies forecasting at NOAA/NCEP – Part 2: Evaluation of aerosol optical thickness. *Geoscientific Model Development*, *11*(6), 2333–2351. https://doi.org/10.5194/gmd-11-2333-2018

Benedetti, A., Morcrette, J. J., Boucher, O., Dethof, A., Engelen, R. J., Fisher, M., Flentje, H., Huneeus, N., Jones, L., Kaiser, J. W., Kinne, S., Mangold, A., Razinger, M., Simmons, A. J., & Suttie, M. (2009). Aerosol analysis and forecast in the European Centre for Medium-Range Weather Forecasts integrated forecast system: 2. data assimilation. *Journal of Geophysical Research Atmospheres*, *114*(13). https://doi.org/10.1029/2008JD011115

Benedetti, A., & Vitart, F. (2018). Can the direct effect of aerosols improve subseasonal predictability? *Monthly Weather Review*, *146*(10), 3481–3498. https://doi.org/10.1175/MWR-D-17-0282.1

Bozzo, A., Benedetti, A., Flemming, J., Kipling, Z., & Rémy, S. (2020). An aerosol climatology for global models based on the tropospheric aerosol scheme in the Integrated Forecasting System of ECMWF. *Geoscientific Model Development*, *13*(3), 1007–1034. https://doi.org/10.5194/gmd-13-1007-2020

Free, M., Sun, B., & Yoo, H. L. (2016). Comparison between total cloud cover in four reanalysis products and cloud measured by visual observations at U.S. weather stations. Journal of Climate, 29(6), 2015–2021. https://doi.org/10.1175/JCLI-D-15-0637.1

Gong, S. L., Lavoué, D., Zhao, T. L., Huang, P., & Kaminski, J. W. (2012). GEM-AQ/EC, an on-line global multi-scale chemical weather modelling system: model development and evaluation of global aerosol climatology. *Atmospheric Chemistry and Physics*, *12*(17), 8237–8256. https://doi.org/10.5194/acp-12-8237-2012

Grell, G. A., S. E. Peckham, R. Schmitz, S. A. McKeen, G. Frost, W. C. Skamarock, and B. Eder, (2005) Fully coupled "online" chemistry within the WRF model. Atmos. Environ., 39, 6957–6975. https://doi.org/10.1016/j.atmosenv.2005.04.027

Hansen, J., Sato, M., & Ruedy, R. (1997). Radiative forcing and climate response. *Journal of Geophysical Research: Atmospheres*, *102*(D6), 6831–6864. https://doi.org/10.1029/96JD03436

Haywood, J., & Boucher, O. (2000). Estimates of the direct and indirect radiative forcing due to tropospheric aerosols: A review. *Reviews of Geophysics*, *38*(4), 513–543. https://doi.org/10.1029/1999RG000078

Hersbach, H., Bell, B., Berrisford, P., Hirahara, S., Horányi, A., Muñoz-Sabater, J., … Thépaut, J. (2020). The ERA5 global reanalysis. Quarterly Journal of the Royal Meteorological Society, 146(730), 1999–2049. https://doi.org/10.1002/qj.3803

Hess, M., Koepke, P., & Schult, I. (1998). Optical Properties of Aerosols and Clouds: The Software Package OPAC. *Bulletin of the American Meteorological Society*, *79*(5), 831–844. https://doi.org/10.1175/1520-0477(1998)079<0831:OPOAAC>2.0.CO;2

Huang, X., Wang, Z., & Ding, A. (2018). Impact of Aerosol-PBL Interaction on

Haze Pollution: Multiyear Observational Evidences in North China. *Geophysical Research Letters*, *45*(16), 8596–8603. https://doi.org/10.1029/2018GL079239

Huang, X., & Ding, A. (2021). Aerosol as a critical factor causing forecast biases of air temperature in global numerical weather prediction models. *Science Bulletin*, *66*(18), 1917–1924. https://doi.org/10.1016/j.scib.2021.05.009

IPCC (2021). Summary for Policymakers. In: Climate Change 2021: The Physical Science Basis. Contribution of Working Group I to the Sixth Assessment Report of the Intergovernmental Panel on Climate Change [MassonDelmotte, V., P. Zhai, A. Pirani, S.L. Connors, C. Péan, S. Berger, N. Caud, Y. Chen, L. Goldfarb, M.I. Gomis, M. Huang, K. Leitzell, E. Lonnoy, J.B.R. Matthews, T.K. Maycock, T. Waterfield, O. Yelekçi, R. Yu, and B. Zhou (eds.)]. Cambridge University Press. In Press.

Japan Meteorological Agency (2002). Annual WWW Technical Progress Report on the Global Data Processing System, *GDPS Technical Progress Report Series*, 12, WMO/TD-No. 1148- 21.03.03.

Japan Meteorological Agency, 2019: Improvement and prospect of Global Spectral Model. *Additonal Volume to Report of Numerical Prediction Division*, 65, 175 pp (in Japanese).

Jeong, G.-R. (2020). Weather Effects of Aerosols in the Global Forecast Model. *Atmosphere*, *11*(8), 850. https://doi.org/10.3390/atmos11080850

Kajino, M., Deushi, M., Sekiyama, T. T., Oshima, N., Yumimoto, K., Tanaka, T. Y., Ching, J., Hashimoto, A., Yamamoto, T., Ikegami, M., Kamada, A., Miyashita, M., Inomata, Y., Shima, S. I., Takami, A., Shimizu, A., & Hatakeyama, S. (2019). NHM-Chem, the Japan meteorological agency's regional meteorology – chemistry model: Model evaluations toward the consistent predictions of the chemical, physical, and optical properties of aerosols. *Journal of the Meteorological Society of Japan*, *97*(2), 337–374. https://doi.org/10.2151/JMSJ.2019-020

Kajino, M., Deushi, M., Sekiyama, T. T., Oshima, N., Yumimoto, K., Tanaka, T. Y., Ching, J., Hashimoto, A., Yamamoto, T., Ikegami, M., Kamada, A., Miyashita, M., Inomata, Y., Shima, S., Khatri, P., Shimizu, A., Irie, H., Adachi, K., Zaizen, Y., Igarashi, Y., Ueda, H., Maki, T., & Mikami, M. (2021a). Comparison of three aerosol representations of NHM-Chem (v1.0) for the simulations of air quality and climate-relevant variables. *Geoscientific Model Development*, 14(4), 2235–2264. https://doi.org/10.5194/gmd-14-2235-2021

Kajino, M., Tanji, N., & Kuramochi, M. (2021b). Better prediction of surface ozone by a superensemble method using emission sensitivity runs in Japan. *Atmospheric Environment: X*, *12*, 100120. https://doi.org/10.1016/j.aeaoa.2021.100120

Kobayashi, S., Ota, Y., Harada, Y., Ebita, A., Moriya, M., Onoda, H., Onogi, K., Kamahori, H., Kobayashi, C., Endo, H., Miyaoka, K., & Takahashi, K.

(2015). The JRA-55 Reanalysis: General Specifications and Basic Characteristics. *Journal of the Meteorological Society of Japan. Ser. II*, *93*(1), 5–48. https://doi.org/10.2151/jmsj.2015-001

Kolusu, S. R., Marsham, J. H., Mulcahy, J., Johnson, B., Dunning, C., Bush, M., & Spracklen, D. v. (2015). Impacts of Amazonia biomass burning aerosols assessed from short-range weather forecasts. *Atmospheric Chemistry and Physics*, *15*(21), 12251–12266. https://doi.org/10.5194/acp-15-12251-2015

Lohmann, U., & Feichter, J. (2005). Global indirect aerosol effects: a review. *Atmospheric Chemistry and Physics*, *5*(3), 715–737. https://doi.org/10.5194/acp-5-715-2005

Lu, S., da Silva, A., Chin, M., Wang, J., Moorthi, S., Juang, H., Chuang, H.-Y., Tang, Y., Jones, L., Iredell, M., and McQueen, J. (2003). The NEMS GFS Aerosol Component: NCEP's Global Aerosol Forecast System, NCEP Office Note 472, 26 pp.

Maki, T., Tanaka, T. Y., Sekiyama, T. T., & Mikami, M. (2011). The Impact of Ground-Based Observations on the Inverse Technique of Aeolian Dust Aerosol. *Scientific Online Letters on the Atmosphere*, *7*(A), 21–24. https://doi.org/10.2151/sola.7A-006

Miao, H., Wang, X., Liu, Y., & Wu, G. (2019). An evaluation of cloud vertical structure in three reanalyses against CloudSat/cloud-aerosol lidar and infrared pathfinder satellite observations. *Atmospheric Science Letters*, 20(7), 1–9. https://doi.org/10.1002/asl.906

Morcrette, J.-J., Boucher, O., Jones, L., Salmond, D., Bechtold, P., Beljaars, A., Benedetti, A., Bonet, A., Kaiser, J. W., Razinger, M., Schulz, M., Serrar, S., Simmons, A. J., Sofiev, M., Suttie, M., Tompkins, A. M., & Untch, A. (2009). Aerosol analysis and forecast in the European Centre for Medium-Range Weather Forecasts Integrated Forecast System: Forward modeling. *Journal of Geophysical Research*, *114*(D6), D06206. https://doi.org/10.1029/2008JD011235

Mulcahy, J. P., Walters, D. N., Bellouin, N., & Milton, S. F. (2014). Impacts of increasing the aerosol complexity in the Met Office global numerical weather prediction model. *Atmospheric Chemistry and Physics*, *14*(9), 4749–4778. https://doi.org/10.5194/acp-14-4749-2014

National Centers for Environmental Prediction, Environmental Modeling Center (2003). The GFS atmospheric model. *NCEP Office Note*, 442, 14 pp.

Rémy, S., Benedetti, A., Bozzo, A., Haiden, T., Jones, L., Razinger, M., Flemming, J., Engelen, R. J., Peuch, V. H., & Thepaut, J. N. (2015). Feedbacks of dust and boundary layer meteorology during a dust storm in the eastern Mediterranean. *Atmospheric Chemistry and Physics*, *15*(22), 12909–12933. https://doi.org/10.5194/acp-15-12909-2015

Rémy, S., Kipling, Z., Flemming, J., Boucher, O., Nabat, P., Michou, M., Bozzo, A., Ades, M., Huijnen, V., Benedetti, A., Engelen, R., Peuch, V.-H., & Morcrette, J.-J. (2019). Description and evaluation of the tropospheric aerosol scheme in the European Centre for Medium-Range Weather Forecasts (ECMWF) Integrated Forecasting System (IFS-AER, cycle 45R1). *Geoscientific Model Development*, *12*(11), 4627–4659. https://doi.org/10.5194/gmd-12-4627-2019

Rodwell, M. J., & Jung, T. (2008). Understanding the local and global impacts of model physics changes: an aerosol example. *Quarterly Journal of the Royal Meteorological Society*, *134*(635), 1479–1497. https://doi.org/10.1002/qj.298

Sekiyama, T. T., Tanaka, T. Y., Shimizu, A., & Miyoshi, T. (2010). Data assimilation of CALIPSO aerosol observations. *Atmospheric Chemistry and Physics*, *10*(1), 39–49. https://doi.org/10.5194/acp-10-39-2010

Sessions, W. R., Reid, J. S., Benedetti, A., Colarco, P. R., da Silva, A., Lu, S., Sekiyama, T., Tanaka, T. Y., Baldasano, J. M., Basart, S., Brooks, M. E., Eck, T. F., Iredell, M., Hansen, J. A., Jorba, O. C., Juang, H.-M. H., Lynch, P., Morcrette, J.-J., Moorthi, S., … Westphal, D. L. (2015). Development towards a global operational aerosol consensus: basic climatological characteristics of the International Cooperative for Aerosol Prediction Multi-Model Ensemble (ICAP-MME). *Atmospheric Chemistry and Physics*, *15*(1), 335–362. https://doi.org/10.5194/acp-15-335-2015

Sugimoto, N., Hara, Y., Yumimoto, K., Uno, I., Nishikawa, M., & Dulam, J. (2010). Dust Emission Estimated with an Assimilated Dust Transport Model Using Lidar Network Data and Vegetation Growth in the Gobi Desert in Mongolia. *SOLA*, *6*(1), 125–128. https://doi.org/10.2151/sola.2010-032

Swinbank, R., Kyouda, M., Buchanan, P., Froude, L., Hamill, T. M., Hewson, T. D., Keller, J. H., Matsueda, M., Methven, J., Pappenberger, F., Scheuerer, M., Titley, H. A., Wilson, L., & Yamaguchi, M. (2016). The TIGGE Project and Its Achievements. *Bulletin of the American Meteorological Society*, *97*(1), 49–67. https://doi.org/10.1175/BAMS-D-13-00191.1

Tanaka, T. Y., Orito, K., Sekiyama, T. T., Shibata, K., Chiba, M., & Tanaka, H. (2003). MASINGAR, a global tropospheric aerosol chemical transport model coupled with MRI/JMA98 GCM: Model description. *Papers in Meteorology and Geophysics*, *53*(4), 119–138. https://doi.org/10.2467/mripapers.53.119

Tanaka, T. Y., & Chiba, M. (2005). Global simulation of dust aerosol with a chemical transport model, MASINGAR. *Journal of the Meteorological Society of Japan*, *83*(3), 255–278. https://doi.org/10.2151/jmsj.83a.255

Tegen, I., Hollrig, P., Chin, M., Fung, I., Jacob, D., & Penner, J. (1997). Contribution of different aerosol species to the global aerosol extinction optical thickness: Estimates from model results. *Journal of Geophysical Research: Atmospheres*, *102*(D20), 23895–23915. https://doi.org/10.1029/97JD01864

Toon, O. B., & Pollack, J. B. (1976). A Global Average Model of Atmospheric Aerosols for Radiative Transfer Calculations. *Journal of Applied Meteorology*, *15*(3), 225–246. https://doi.org/10.1175/1520-0450(1976)015<0225:AGAMOA>2.0.CO;2

Thorsen, T. J., Ferrare, R. A., Kato, S., & Winker, D. M. (2020). Aerosol Direct Radiative Effect Sensitivity Analysis. *Journal of Climate*, *33*(14), 6119–6139. https://doi.org/10.1175/JCLI-D-19-0669.1

Vitart, F., Ardilouze, C., Bonet, A., Brookshaw, A., Chen, M., Codorean, C., Déqué, M., Ferranti, L., Fucile, E., Fuentes, M., Hendon, H., Hodgson, J., Kang, H. S., Kumar, A., Lin, H., Liu, G., Liu, X., Malguzzi, P., Mallas, I., … Zhang, L. (2017). The Subseasonal to Seasonal (S2S) Prediction Project Database. *Bulletin of the American Meteorological Society*, *98*(1), 163–173. https://doi.org/10.1175/BAMS-D-16-0017.1

Vitart, F., & Robertson, A. W. (2018). The sub-seasonal to seasonal prediction project (S2S) and the prediction of extreme events. *Npj Climate and Atmospheric Science*, *1*(1), 3. https://doi.org/10.1038/s41612-018-0013-0

White, C. J., Carlsen, H., Robertson, A. W., Klein, R. J. T., Lazo, J. K., Kumar, A., Vitart, F., Coughlan de Perez, E., Ray, A. J., Murray, V., Bharwani, S., MacLeod, D., James, R., Fleming, L., Morse, A. P., Eggen, B., Graham, R., Kjellström, E., Becker, E., … Zebiak, S. E. (2017). Potential applications of subseasonal-to-seasonal (S2S) predictions. *Meteorological Applications*, *24*(3), 315–325. https://doi.org/10.1002/met.1654

Woodward, S. (2001). Modeling the atmospheric life cycle and radiative impact of mineral dust in the Hadley Centre climate model. *Journal of Geophysical Research: Atmospheres*, *106*(D16), 18155–18166. https://doi.org/10.1029/2000JD900795

Yamagami, A., & Matsueda, M. (2020). Subseasonal Forecast Skill for Weekly Mean Atmospheric Variability Over the Northern Hemisphere in Winter and Its Relationship to Midlatitude Teleconnections. *Geophysical Research Letters*, *47*(17), 1–9. https://doi.org/10.1029/2020GL088508

Yamagami, A., Matsueda, M., & Tanaka, H. L. (2018). Medium-range forecast skill for extraordinary Arctic cyclones in summer of 2008–2016. *Geophysical Research Letters*, *45*(9), 4429–4437. https://doi.org/10.1029/2018GL077278

Yamagami, A., & Matsueda, M. (2021). Statistical characteristics of Arctic forecast busts and their relationship to Arctic weather patterns in summer. *Atmospheric Science Letters*, *March*. https://doi.org/10.1002/asl.1038

Yukimoto, S., H. Yoshimura, M. Hosaka, T. Sakami, H. Tsujino, M. Hirabara, T. Y. Tanaka, M. Deushi, A. Obata, H. Nakano, Y. Adachi, E. Shindo, S. Yabu, T. Ose, and A. Kitoh, (2011). Meteorological Research Institute Earth System Model Version 1 (MRI-ESM1)—Model Description—. *Tech. Rep. of MRI*, 64, 83 pp.

Yukimoto, S., Adachi, Y., Hosaka, M., SAKAMI, T., YOSHIMURA, H., HIRABARA, M., TANAKA, T. Y., SHINDO, E., TSUJINO, H., DEUSHI, M., MIZUTA, R., YABU, S., OBATA, A., NAKANO, H., KOSHIRO, T., OSE, T., & KITOH, A. (2012). A New Global Climate Model of the Meteorological Research Institute: MRI-CGCM3 —Model Description and Basic Performance—. *Journal of the Meteorological Society of Japan. Ser. II*, *90A*(A), 23–64. https://doi.org/10.2151/jmsj.2012-A02

Yumimoto, K., Uno, I., Sugimoto, N., Shimizu, A., Liu, Z., & Winker, D. M. (2008). Adjoint inversion modeling of Asian dust emission using lidar observations. *Atmospheric Chemistry and Physics*, *8*(11), 2869–2884. https://doi.org/10.5194/acp-8-2869-2008

Yumimoto, K., Nagao, T. M., Kikuchi, M., Sekiyama, T. T., Murakami, H., Tanaka, T. Y., Ogi, A., Irie, H., Khatri, P., Okumura, H., Arai, K., Morino, I., Uchino, O., & Maki, T. (2016). Aerosol data assimilation using data from Himawari-8, a next-generation geostationary meteorological satellite. *Geophysical Research Letters*, *43*(11), 5886–5894. https://doi.org/10.1002/2016GL069298

Yumimoto, K., Tanaka, T. Y., Oshima, N., & Maki, T. (2017). JRAero: the Japanese Reanalysis for Aerosol v1.0. *Geoscientific Model Development*, *10*(9), 3225–3253. https://doi.org/10.5194/gmd-10-3225-2017

Zhang, J., Reid, J. S., Christensen, M., & Benedetti, A. (2016). An evaluation of the impact of aerosol particles on weather forecasts from a biomass burning aerosol event over the Midwestern United States: observational-based analysis of surface temperature. *Atmospheric Chemistry and Physics*, *16*(10), 6475–6494. https://doi.org/10.5194/acp-16-6475-2016

Zhou, L., Lin, S.-J., Chen, J.-H., Harris, L. M., Chen, X., & Rees, S. L. (2019). Toward Convective-Scale Prediction within the Next Generation Global Prediction System. *Bulletin of the American Meteorological Society*, *100*(7), 1225–1243. https://doi.org/10.1175/BAMS-D-17-0246.1

Zhou, X., and others (2021). The Introduction of the NCEP Global Ensemble Forecast System 779 Version 12, in preparation.